Brillouin Scattering in Long-Scale-Length Laser Plasmas

The experimental study of parametric instabilities in long-scale-length laser plasmas is very important for inertial confinement fusion (ICF). Backscattered light near the incident light wavelength has been observed in many laser-plasma experiments and is generally attributed to stimulated Brillouin scattering (SBS).[1,2] Stimulated Brillouin scattering is a parametric instability in which an incident electromagnetic wave decays into another electromagnetic wave and an ion-acoustic wave.[3,4] The instability can grow over a large volume of plasma when $n_e < n_{cr}$, where n_e and n_{cr} are the electron and critical densities, respectively. (Here n_{cr} indicates the critical density for 1054-nm laser light.) Stimulated Brillouin scattering in future, long-scale-length ICF plasmas may be significant and could pose problems for efficient coupling of laser light to ICF targets.

SBS has been studied extensively in the past, both experimentally[5–9] and theoretically.[4,10,11] At the present time, there is little or no agreement between observed SBS reflectivities and theoretical predictions based on the assumption that SBS grows convectively from thermal noise fluctuations.[12,13]

We present here a series of 1054-nm interaction experiments on Brillouin scattering carried out on long-scale-length laser plasmas produced with the 24-beam OMEGA laser facility at the Laboratory for Laser Energetics, which has subsequently been upgraded to a 60-beam, 45-kJ at 351-nm laser. We have observed time-resolved Brillouin spectra and measured the total backscattered energy. We attempt to explain these data on the basis of existing SBS theory in inhomogeneous plasmas, hydrodynamic simulations of the background plasma, and statistically described intensity distributions of the interaction beam. An important result is that the plasma-density-gradient scale length $L_n = n_e\left(dn_e/dx\right)^{-1}$, after the foil burns through, approaches that expected in proposed ICF targets ($L_n \sim 1$ mm).

In the following sections we describe the experimental arrangement (geometry, target conditions, and measurement techniques), present the experimental data, discuss the numerical SBS calculations, and finally, give a detailed comparison of experimental data and calculated results.

Experimental Description

The long-scale-length, preformed plasma of these experiments was produced by exploding mass-limited CH foil targets of 6-μm thickness and 600-μm diameter overcoated with 500 Å of Al. The geometry of the experiment showing the beams and diagnostics is shown in Fig. 67.1.[5,6] Eight primary beams peaking at time 1.0 ns were followed by eight secondary beams (Fig. 67.2), peaking at 1.6 ns (i.e., delayed by 0.6 ns from the primary beams) to maintain the electron temperature $T_e > 1$ keV over a time period of 0.5 ns. The primary and secondary beams ($\lambda = 351$ nm) had an on-target energy of ~50 to 60 J each with a pulse duration of ~0.6 ns. All beams were outfitted with distributed phase plates (DPP, element size = 1.25 mm) producing a minimum spot size at the best focus of 163-μm FWHM. All beams were defocused to ~450-μm FWHM to illuminate the target uniformly with an intensity of $\sim 5 \times 10^{13}$ W/cm^2 per beam. More detailed information about the production and characterization of the background plasma and its properties can be found in Ref. 6.

The preformed plasma was then irradiated by one of the OMEGA beams at $\lambda_0 = 1054$ nm with on-target energy of ~50 J in a pulse width of 0.7-ns FWHM. This interaction beam was incident on the target at ~60° with respect to the target normal. The timing between the beginning of the heating beams and the peak of the interaction beam was varied between 2.2 and 3.7 ns (see Fig. 67.2) to access different plasma conditions. The interaction beam was propagated through a phase plate with 3-mm cells to produce a focal spot of 210-μm FWHM, giving a maximum intensity on target, averaged over many DPP speckles, of $\sim 1.3 \times 10^{14}$ W/cm^2. At the time of the peak of the earliest interaction beam (2.2 ns), the produced target plasma had a center density of 1 to 2×10^{21} cm^{-3}, which was maintained within a factor of 2 at $T_e \sim 1$ keV for approximately 1 ns. The corresponding density-gradient scale length was typically of the order of 1 mm for all timings.

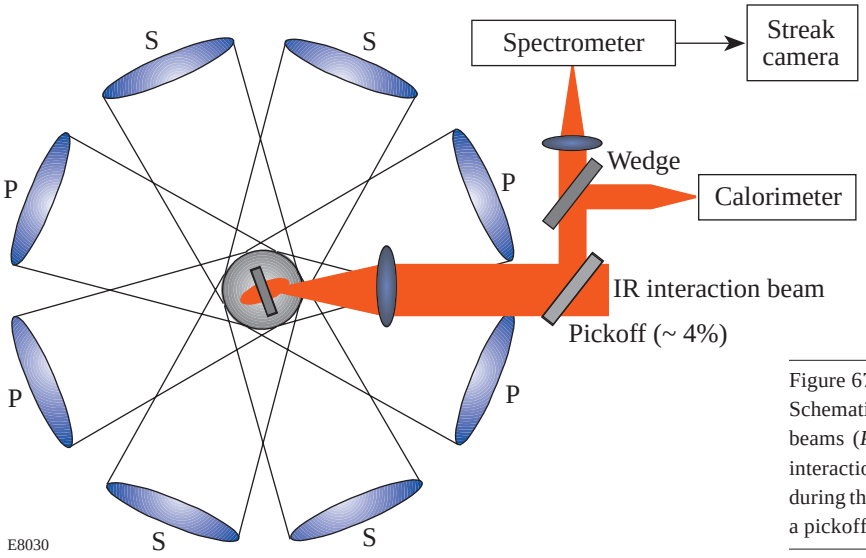

Figure 67.1
Schematic arrangement of the SBS experiments. Eight primary beams (*P*) are followed by eight secondary beams (*S*). The IR interaction beam is delayed to vary the specific plasma conditions during the interaction time. The backscattered signal is directed by a pickoff into a spectrometer/streak camera and a calorimeter.

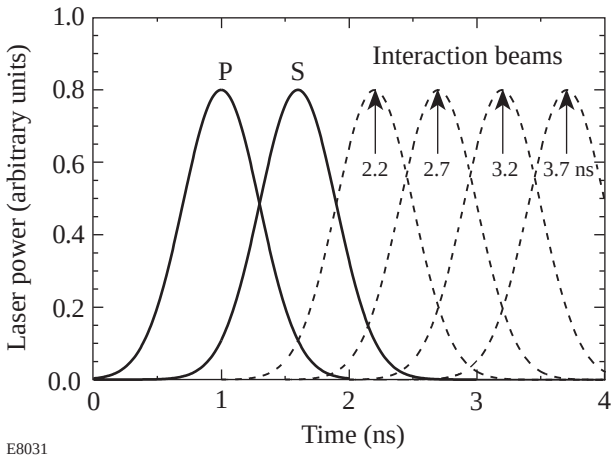

Figure 67.2
Relative timing of the primary (*P*), secondary (*S*), and interaction beams. The peak of the intensity envelope of the primary and secondary UV beams is around 2×10^{13} W/cm^2 averaged over many DPP speckles, while the peak of the intensity envelope of the interaction beam is 1.3×10^{14} W/cm^2 (also averaged over many speckles). The timing of the peak of the interaction beam was varied between 2.2 and 3.7 ns in 0.5-ns increments.

The primary diagnostic for the scattered light near λ_0 consisted of a 1-m grating SPEX spectrometer coupled to an optical streak camera (see Fig. 67.1). The backscattered light was directed by an uncoated pickoff through the lens into the spectrometer and streak camera with 5-Å spectral resolution and 30-ps time resolution, respectively. The streak camera data was recorded on film and photodensitometered for the subsequent analysis. An RG1000 filter was used to protect the streak camera against 527- and 351-nm laser light. A set of neutral density filters was installed in front of the spectrometer slit to attenuate reflected light. Part of the reflected beam was used to measure the total energy of the backscattered light within the focusing cone of the interaction beam, using an IR calorimeter (Fig. 67.1).

Experimental Results

Typical time-resolved backscattered spectra are shown in Fig. 67.3 for three different timings τ_d of the interaction beam (2.2, 2.7, and 3.2 ns). The interaction intensity averaged over many DPP speckles was about 1.3×10^{14} W/cm^2. The time delay provides a flexible way to vary the plasma conditions seen by the interaction beam. Backscattered spectra show a few general features. First, the backscattered light is primarily blue-shifted with respect to the incident wavelength λ_0. Second, all spectra shift to shorter wavelengths with time. The width of the spectrum is typically $\Delta\omega/\omega_0 \sim 0.01$, and the total emission basically lasts up to 600 ps for all timings.

Figure 67.3(a) shows the backscattered spectrum for a timing of 2.2 ns. The width of the spectrum is about 30 Å and starts 400 ps before the peak of the pulse. This spectrum has additional spectral features: a narrow, slightly blue-shifted, spectral component preceding the interaction beam peak and the presence of a weak red-shifted component. The narrow, slightly blue-shifted component is probably due to the scattered light from the secondary heating beams, which also contain residual energy at 1054 nm left over from incomplete frequency conversion.

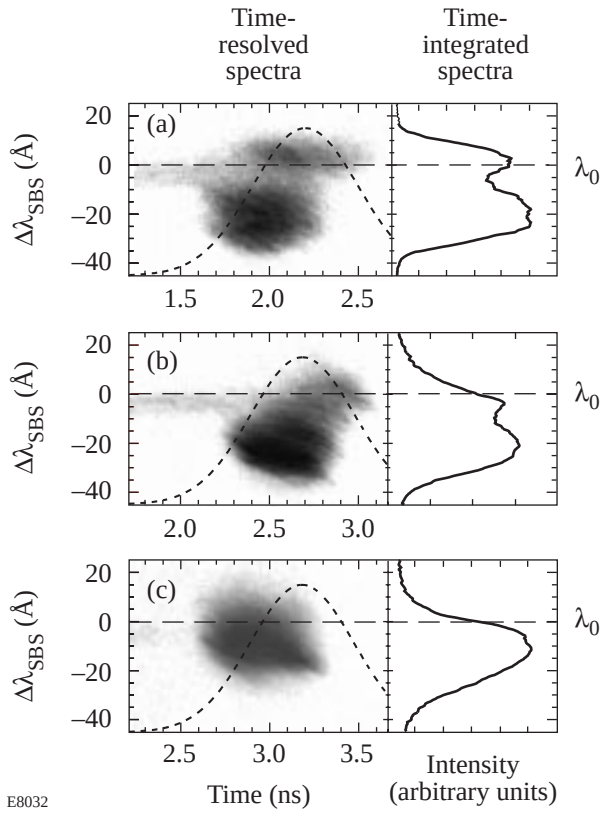

Figure 67.3
Streaked backscattered light from a CH target. The interaction beam peaks at (a) 2.2 ns, (b) 2.7 ns, and (c) 3.2 ns as indicated by the dashed curves.

A slightly red-shifted component is a feature observed only for the shortest timing of the interaction beam (2.2 ns). This component has an ~8-Å spectral width and appears later than the main blue-shifted component. The intensity of this component is about 20% less than that for the blue-shifted one. A fine spectral pattern can be noted in both components of the spectrum. This pattern is inclined to the time axis, giving the impression of lines consistently shifting toward the blue with increasing time.

The backscattered spectrum shown in Fig. 67.3(b) is for a delay of 2.7 ns. Unlike the spectrum in Fig. 67.3(a), we see mostly the blue component, which starts ~300 ps before the peak and lasts up to 600 ps. Some signal is still observed at 0 Å and the fine spectral structure becomes less visible. Finally, Fig. 67.3(c) shows the backscattered spectrum for 3.2-ns timing. It exhibits only a blue-shifted component peaked at –10 Å. The entire spectrum is less blue-shifted, starting about 400 ps before the peak and stopping 200 ps after the peak. The fine spectral structure has basically disappeared for this timing.

A plot of the measured time-integrated reflectivity of the backscattered light versus timing τ_d of the interaction beam is shown in Fig. 67.4 (solid squares). A slow decrease of Brillouin light with increased timing was observed with values between 10% for the shortest timing (2.2 ns) and 1% for the longest timing (3.7 ns). The numerical predictions indicate that the electron density n_e in the interaction region decreases from ~0.9 n_{cr} (t = 2.2 ns) to ~0.03 n_{cr} (t = 3.7 ns).

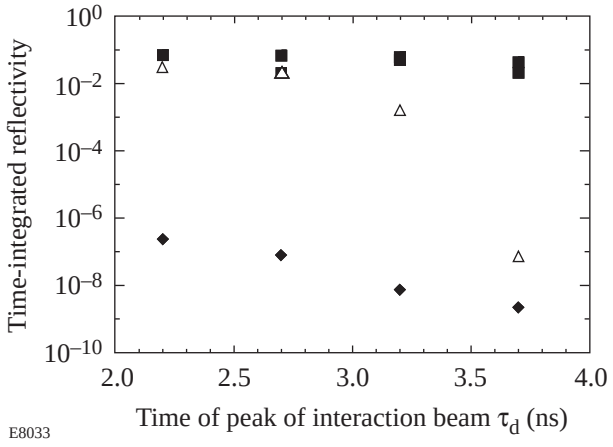

Figure 67.4
Time-integrated reflectivity R as a function of time delay of the interaction beam. Squares (■) are experimental data; triangles (△) represent the time-integrated reflectivity calculated using Eq. (7) including a hot-spot model; and diamonds (◆) show the total reflectivity based only on the peak of the intensity envelope (1.3×10^{14} W/cm^2).

Theory and Simulations

In the following discussion we assume that backscattered light, at wavelengths close to that of the laser, is a consequence of the onset of the conventional SBS instability. While the resultant scattered light would be red-shifted in a quiescent plasma, our experimental plasma has supersonic flow present, which could account for the observed blue shifts. Accordingly, we calculate the scattered intensity and spectrum using conventional linear three-wave convective SBS theory.

Assuming one-dimensional (spherical) geometry, the scattered flux growing from electrostatic ion-wave thermal fluctuations (the dominant noise source) is given by a modified form of Eq. (25) in Ref. 12. For backscatter, this yields

$$F_L = \frac{cT_e}{\lambda_s^4}\,\frac{\omega_s}{2(\omega_0-\omega_s)}\left[e^{G(\omega_s)}-1\right], \qquad (1)$$

where F_L is the flux of scattered radiation per unit solid angle per unit vacuum wavelength λ_s, and T_e is the electron temperature.

A useful expression for the gain G is given in Ref. 10. This has the form

$$G = \frac{1}{4}\int_a^b k^2 \frac{v_0^2}{c^2|k_s|}\,\mathrm{Im}\left[\frac{\chi_e(\chi_i+1)}{\varepsilon(k,\omega)}\right]dx. \qquad (2)$$

Here $\mathbf{k} = \mathbf{k}_0 - \mathbf{k}_s$, $\chi_e(k,\omega)$, and $\chi_i(k,\omega)$ are the low-frequency electron and ion susceptibilities, respectively, with $\omega = \omega_0 - \omega_s$, $\varepsilon = 1 + \chi_e(k,\omega) + \chi_i(k,\omega)$, and v_0 is the peak quiver velocity $\left[v_0^2(t) \propto I(t)\right]$ of the electrons due to the interaction beam. The wave vectors $\mathbf{k}_0$, $\mathbf{k}_s$, and $\mathbf{k}$ are the local values for the incident and scattered electromagnetic waves and the ion waves, and $c^2k_{0,s}^2 = \omega_{0,s}^2 - \omega_{\mathrm{pe}}^2$. The integration in Eq. (2) is taken across a finite inhomogeneous plasma from point $x = a$ at the rear of the plasma (the opposite side from the interaction beam) up to $x = b$, which is in the vacuum on the laser side. Both the full spectrum and the reflectivity are obtained by including all scattered frequencies. The temporal evolution of G is determined by the temporal evolution of the intensity and the plasma parameters in the interaction region. The spatial speckle distribution in the interaction beam created by the distributed phase plate can be taken into account by appropriate averaging of the backscattered SBS energy over the intensity distribution.

Application of Eq. (2) to our experiment is made by numerical integration. The temporal evolution of the background plasma properties (plasma temperature, density, and flow velocity) is obtained from simulations using the 2-D hydrodynamic code *SAGE* in cylindrical geometry. We model the interaction beam as a finite cylinder striking the target normally, while in the actual experiment the interaction beam enters at a considerable angle (~60°) to the normal. However, rapid plasma expansion, prior to the onset of the interaction beam, produces a near-spherical plasma cloud that justifies our simplified modeling.

A typical result of this *SAGE* simulation is shown in Fig. 67.5 for time $t = 2.2$ ns (the peak of the interaction beam is also at 2.2 ns in this simulation). The values shown are along the central axis of the beam. At this time, part of the plasma is still overdense to the laser beam, the density-gradient scale length L_n is of the order of 600 μm, and the velocity-gradient scale length L_v is of the order of 400 μm. Peak densities of $n_e > n_{\mathrm{cr}}$ are present for the shorter delays, while interaction beams with the longest delays encounter a plasma with peak densities below $0.03\,n_{\mathrm{cr}}$. The interaction beam sees an electron temperature varying between $T_e \approx 0.4$ and 1.2 keV. The local Mach numbers (expansion velocities) are close to zero near the plasma center and increase to $M \approx 3$ to 3.5 at the plasma edge. The interaction beam intensity decreases smoothly with penetration distance, owing to inverse Bremsstrahlung, and is virtually negligible after reflection from the critical surface. It is worth pointing out that at early times the interaction beam sees only regions with supersonic flow, while later in time it will propagate through both supersonic and subsonic regions of flowing plasma.

In our numerical integration, we assumed that

$$\chi_e(k) \cong \left(k^2\lambda_D^2\right)^{-1} >> 1 \qquad (3)$$

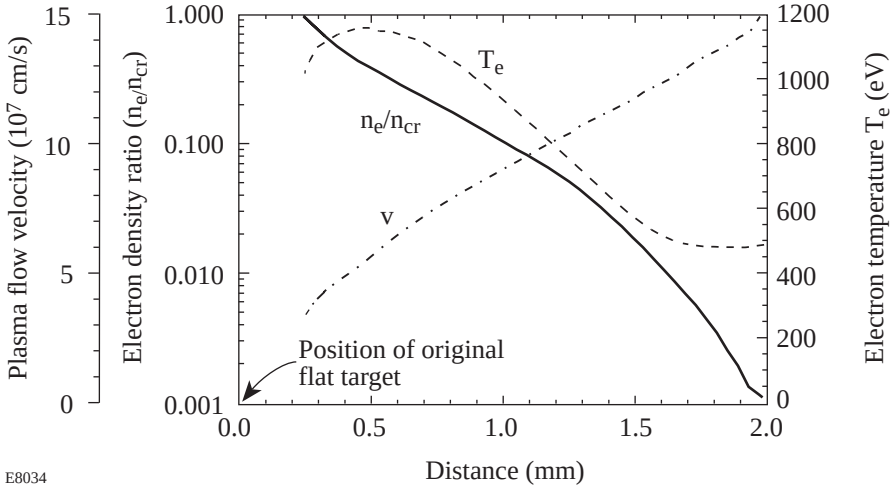

Figure 67.5
Calculated *SAGE* profiles of the relative density n_e/n_{cr}, the plasma expansion velocity v, and the electron temperature T_e for a mass-limited CH target. The peak of the interaction beam is at 2.2 ns. The velocity- and density-gradient scale lengths are $L_v \approx 400$ μm and $L_n \approx 600$ μm, respectively.

and

$$\chi_i(k,\omega) \cong -\frac{\omega_{\mathrm{pi}}^2}{\left(\omega - i\gamma - \mathbf{k}\cdot\mathbf{v}\right)^2}. \tag{4}$$

Here λ_D is the usual Debye length, ω_{pi} is the ion plasma frequency, and $\mathbf{v}$ is the plasma flow velocity. Damping has been included through the addition of an imaginary component γ to the frequency. Generally, we neglect electron Landau damping of the ion waves, and thus χ_e is real. The damping term in χ_i is chosen as a sum of the Landau damping of the ion waves and a collisional contribution. However, since the integrand in our integration over x is strongly resonant about a matching point $x_m(\lambda_s)$, where $\mathrm{Re}\left[\varepsilon\left(x_m\right)\right] = 0$, it turns out that the resultant integral is very insensitive to the precise form chosen for γ (this is a well-known result). We have carried out additional calculations that included electron Landau damping and found only negligible corrections to our previous results.

Since G enters in an exponential in the expression for the scattered intensity, we expect a strong dependence of the total reflectivity on time delay. This is borne out by the theoretical result shown in Fig. 67.4. These solid diamonds (◆) are the calculated reflectivity based on using the average interaction intensity in the exponent. We see more than six-orders-of-magnitude difference between theory and experiment for a time delay of 3.7 ns. As the delay decreases, G increases and the theoretical curve and experimental data approach each other but still remain far apart. This major discrepancy between experiment and the conventional SBS convective theory is not new. It has been noted previously in a series of experiments covering short, intermediate, and long pulse lengths for the interaction beam.[11,13,14] It seems clear that conventional convective SBS theory has great difficulty accounting for the measurements of backscattered radiation at frequencies close to that of the laser.

Since the intensity I appears in the exponential, we have considered whether spatial nonuniformities in the actual beam would substantially change the calculated SBS reflectivities. Inclusion of a statistical distribution of the laser-light intensity in our calculations has yielded an overall increase in G of the order of 2 or more. While this correction has a profound effect on the calculated SBS reflectivities for the shorter time delays, for which G is large (G is of the order of 10 to 20), it has little effect when G is small.

The calculation incorporating statistical nonuniformities of the actual beam was carried out as follows. From a numerical analysis of the speckles produced by the DPP at the target plane, we obtained a probability distribution of the intensity. This probability distribution and its running integral as a function of intensity are shown in Fig. 67.6. From this plot one can find the fraction of total intensity in the beam that is at or below a given intensity. This probability distribution was based on an area outlined by the FWHM (210 μm) of the distribution and containing ~50% of the total incident energy. In the actual calculations, we used an analytical fit[15] to the probability distribution:

$$P_{\mathrm{fit}}(I) = \frac{1}{I_{\mathrm{av}}}\exp\left(-\frac{I}{I_{\mathrm{av}}}\right), \tag{5}$$

where $I_{\mathrm{av}} = 1.3 \times 10^{14}$ W/cm^2. This is a very good fit, as is shown in Fig. 67.6.

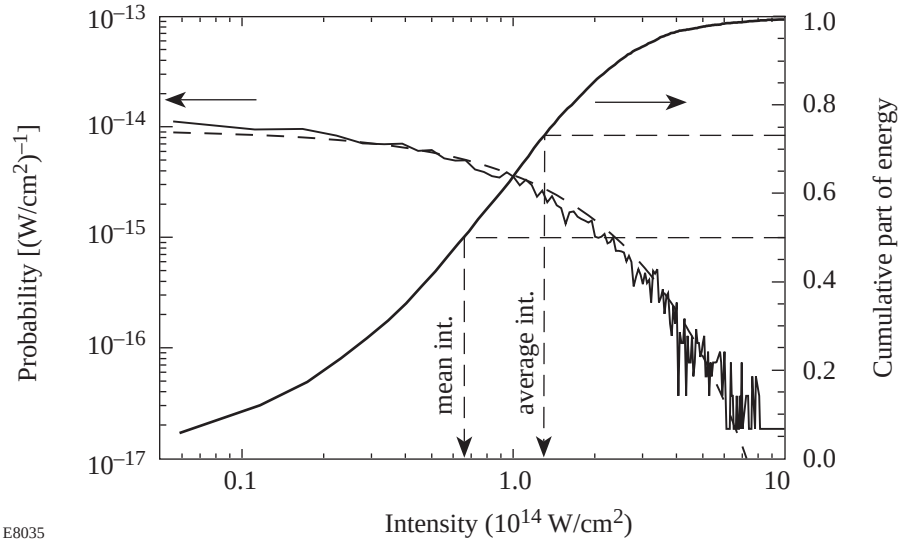

Figure 67.6
The probability distribution of the intensity of the interaction beam in the focal plane and its cumulative fraction. The dashed line shows the analytical fit given by Eq. (5).

The instantaneous flux of backscattered radiation through a solid angle $\Delta\Omega = 0.06$ sr (the solid angle subtended by the entire focusing lens) is obtained by integrating Eq. (1) over wavelength:

$$\Phi_{\mathrm{SBS}}(I,t) = \Delta\Omega \times \int_{\lambda} F_L \, d\lambda . \tag{6}$$

The time-integrated reflectivity R_{SBS} is then defined as

$$R_{\mathrm{SBS}} \equiv \frac{E_{\mathrm{SBS}}}{E_{\mathrm{in}}} = \frac{\int_t \int_I \Phi_{\mathrm{SBS}}(I,t)\, P(I,t)\, dI dt}{\int_t \int_I I(t)\, P(I,t)\, dI dt}. \tag{7}$$

The quantities E_{SBS} and E_{in} denote the backscattered and incident energy, respectively. Using this model to calculate the reflectivity yielded the triangles (△) shown in Fig. 67.4. For the highest gains it was necessary to include pump depletion to avoid instantaneous reflectivities of >100% for the largest intensity components.

The resultant predictions for the reflectivity are now in reasonable agreement with the experimental results for short time delays (where $n_e \sim 0.7$–$0.9\, n_{\mathrm{cr}}$) but strongly disagree for the later timings ($n_e \le 0.03\, n_{\mathrm{cr}}$). We found that for the shortest timings (2.2 ns) the calculated gains for the peak reflected wavelength are ~10 during the major part of the pulse. As the time delay increases, the gain decreases monotonically and becomes of the order of 1 to 2 for a delay of 3.2 ns.

While the precise dependence of G on the density and flow velocity is rather complex, we can obtain a qualitative understanding of the variation of G from an approximate analytic treatment. In the weak damping limit, there is a sharp resonance in the integrand of Eq. (2) at the resonance point, x_m, at which $\mathrm{Re}\left[\varepsilon\left(x_m\right)\right] = 0$. Carrying out the resonant integration in x, the expression for the gain becomes[4]

$$G \cong \frac{\dfrac{\pi}{4}\left(\dfrac{v_0}{v_e}\right)^2 \dfrac{n_e}{n_c} k_0 L_v}{\left|\left(\dfrac{n_e}{n_c}\right)\left(\dfrac{L_v}{L_n}\right)(1-M) - 2M\left(1-\dfrac{n_e}{n_c}\right)\right|}, \tag{8}$$

where M denotes the Mach number, $L_n = n_e \big/ \left(dn_e/dx\right)$ is the density-gradient scale length, L_v is velocity-gradient scale length, and all quantities are evaluated at x_m. This result agrees exactly with the expression given in Ref. 4 if one neglects the temperature gradient (as seems appropriate for our plasma) and allows for our definition of $L_v = v\left(dv/dx\right)^{-1}$.

At the matching point, one has $\omega_0 - \omega_s - \mathbf{k}\cdot\mathbf{v} \approx kc_s$, where c_s is the sound speed, and, since $k \approx 2k_0$, this has the form $\omega_0 - \omega_s - 2\,\mathbf{k}_0 \cdot \mathbf{v}\left(x_m\right) \approx 2\,kc_s$. Roughly, for a particular scattered frequency ω_s, the matching point is at a specific value of the flow velocity. As the time delay increases, we note that a given velocity moves farther out in space. The density at that point also has dropped; hence, it becomes clear why the gain decreases with increasing time delay.

The possibility that the dominant reflected beam is the phase conjugate of the laser beam has generated considerable interest. We note that phase conjugation can at most yield a factor-of-2 increase in the gain over the value obtained using the speckle-averaged intensity.[16] Once again, this will have little effect on the large discrepancy between theory and experiment for the longer time delays.

Equation (2) also allows us to predict the scattered spectrum as a function of time. If we include hot-spot variation via Eq. (5), the resultant calculated streaks (shown in Fig. 67.7) indicate reasonable agreement with the observed experimental streaks (Fig. 67.3). However, note the difference in the time variation of the calculations and the measurements. The red-shifted components seen in the calculated spectra [Figs. 67.7(b) and 67.7(c)] are due to a strong resonance in the gain integral at points close to the center of the plasma, where the expansion velocity is subsonic. With the exception of one shot, we did not see such strongly red-shifted components. This discrepancy is likely due to refraction of the interaction beam. The effect of refraction of the interaction beam is clearly seen in ray-tracing simulations carried out on the 2-D plasma profiles generated by *SAGE*. However, our simulations use only the central ray along the axis of symmetry. For such a ray, by definition, refraction does not occur. We have found no reasonable and satisfactory way to include refraction in our model since ray tracing in this region leads to caustics and crossing rays for which intensities cannot be defined without recourse to physical optics.

Since conventional SBS linear gain theory cannot account apparently for all our observations, one should note other possible explanations. Among the possibilities raised in the

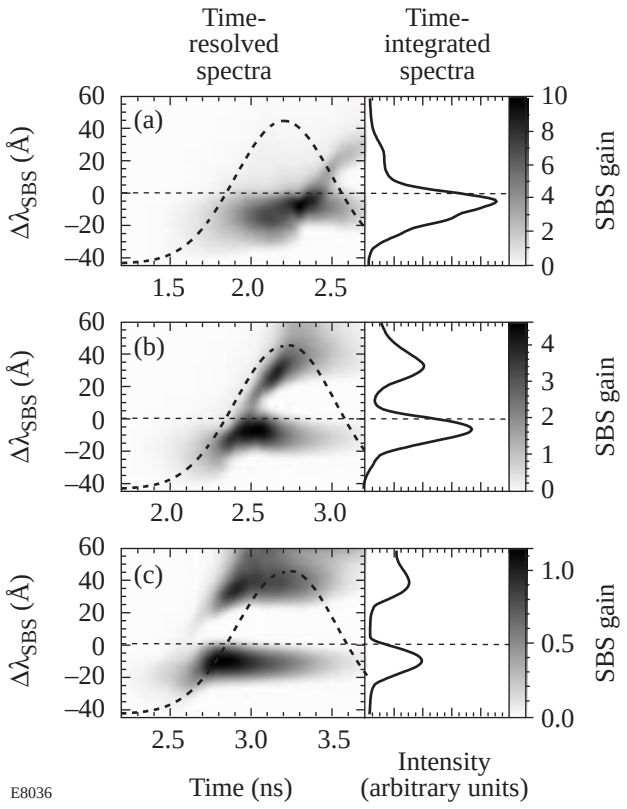

Figure 67.7
Calculated SBS gain as a function of time and spectral shift for three timings of the interaction beam: (a) 2.2 ns, (b) 2.7 ns, and (c) 3.2 ns. Hot-spot variation of the intensity is modeled using Eq. (5), and pump depletion is included.

literature, we call attention to the possible role of filamentation,[17] ion beams,[18,19] and enhanced ion wave noise.[20] In addition, one other explanation should be offered for the relative insensitivity of the SBS signal to the delay time seen in Fig. 67.4. The target is initially exploded by four primary beams from each side, which, when overlapped, produce a pattern that has four minima around the azimuth. Three-dimensional effects associated with these portions disassembling slower than average may result in the maintenance of near-critical densities for longer than predicted by the azimuthally symmetric *SAGE* calculations.

We should note also that we have examined density and velocity perturbations (ripples) that could propagate down the density gradient at the sound velocity in the flowing plasma. Assuming enhanced SBS at the top of such ripples, one can reproduce quite well the slope of the fine structure seen in Fig. 67.3(a). However, for Fig. 67.3(b) the slope of the resultant fine structure differs significantly from the observations. Since it is also difficult to argue how such ripples lead to locally enhanced SBS reflectivities, we conclude that this mechanism is unlikely to account for the observed spectral fine structure.

Summary and Conclusions

We have observed backscattered Brillouin spectra for a range of interaction beam delays corresponding to electron-density changes during the interaction pulse. The blue-shifted spectra of the reflected light are centered mostly near –15 Å. The spectra for the shortest timings also include a slightly red-shifted component. The measured backscattered light reflectivity is in the range of 1%–7%. Calculated SBS reflectivities are in agreement with the measurements for the shortest timings (plasma densities near critical) but are far below the experimental reflectivities for the later timings ($n_e < 0.1\ n_{cr}$). Calculations of the spectra yield a blue shift similar to the observations, but the predicted and observed time variations differ. A calculated red-shifted component is generally not observed in the experiments, a discrepancy that is attributed to refraction of the interaction beam, which is not included in the calculations.

ACKNOWLEDGMENT

This work was supported by the U.S. Department of Energy Office of Inertial Confinement Fusion under Cooperative Agreement No. DE-FC03-92SF19460, the University of Rochester, and the New York State Energy Research and Development Authority. The support of DOE does not constitute an endorsement by DOE of the views expressed in this article.

REFERENCES

1. P. E. Young, H. A. Baldis, and K. G. Estabrook, Phys. Fluids B **3**, 1245 (1991).

2. H. A. Baldis *et al.*, in *Femtosecond to Nanosecond High-Intensity Lasers and Applications*, edited by E. M. Campbell (SPIE, Bellingham, WA, 1990), Vol. 1229, pp. 144–149.

3. M. N. Rosenbluth, Phys. Rev. Lett. **29**, 565 (1972).

4. C. S. Liu, M. N. Rosenbluth, and R. B. White, Phys. Fluids **17**, 1211 (1974).

5. W. Seka, R. S. Craxton, R. E. Bahr, D. L. Brown, D. K. Bradley, P. A. Jaanimagi, B. Yaakobi, and R. Epstein, Phys. Fluids B **4**, 432 (1992).

6. W. Seka, R. E. Bahr, R. W. Short, A. Simon, R. S. Craxton, D. S. Montgomery, and A. E. Rubenchik, Phys. Fluids B **4**, 2232 (1992).

7. H. A. Baldis, E. M. Campbell, and W. L. Kruer, in *Handbook of Plasma Physics*, Physics of Laser Plasma, edited by A. Rubenchik and S. Witkowski (North-Holland, Amsterdam, 1991), Vol. 3, pp. 361–434.

8. R. P. Drake *et al*., Phys. Fluids **31**, 1795 (1988).

9. D. R. Gray *et al*., Plasma Physics **22**, 967 (1980).

10. G. R. Mitchel, T. W. Johnston, and H. Pépin, Phys. Fluids **26**, 2292 (1983).

11. H. A. Baldis *et al*., Phys. Fluids B **5**, 3319 (1993).

12. R. L. Berger, E. A. Williams, and A. Simon, Phys. Fluids B **1**, 414 (1989). Note that Eq. (25) has an obvious misprint; however, it simplifies even further. The derivation carried out in that paper neglected the x-dependence of the group velocity v_{gs}. If this is included, a revised form of Eq. (25) results in which the last bracket is replaced simply by cos Θ. For backscatter, this reduces to our Eq. (1).

13. P. E. Young *et al*., Phys. Fluids B **2**, 1907 (1990).

14. H. A. Baldis *et al*., Lawrence Livermore National Laboratory Inertial Confinement Fusion ICF Quarterly Report UCRL-LR-105821-93-3, 1993 (unpublished), p. 137.

15. H. A. Rose and D. F. DuBois, Phys. Fluids B **5**, 590 (1993).

16. B. Ya. Zel'dovich, N. F. Pilipetsky, and V. V. Shkunov, in *Principles of Phase Conjugation*, Springer Series in Optical Sciences, edited by J. M. Enoch *et al.* (Springer-Verlag, Berlin, 1985), Vol. 42.

17. J. D. Moody *et al*., Phys. Plasmas **2**, 4285 (1995).

18. A. Simon, Bull. Am. Phys. Soc. **38**, 1935 (1993).

19. A. Simon, Bull. Am. Phys. Soc. **40**, 1779 (1995).

20. S. D. Baton *et al*., Phys. Rev. E **49**, R3602 (1994).